IOP Publishing Journal of Physics D: Applied Physics
J. Phys. D: Appl. Phys. **45** (2012) 035202 (9pp) doi:10.1088/0022-3727/45/3/035202

Three-dimensional flow measurements induced from serpentine plasma actuators in quiescent air

R J Durscher and S Roy

Department of Mechanical and Aerospace Engineering, University of Florida, Gainesville, FL 32611, USA

E-mail: roy@ufl.edu

Received 12 August 2011, in final form 11 November 2011
Published 4 January 2012
Online at stacks.iop.org/JPhysD/45/035202

Abstract
This paper presents three-dimensional flow measurements performed on a dielectric barrier discharge (DBD) actuator with the electrodes in a serpentine design. Such a configuration induces a local pinching and a local spreading of the fluid as one follows along the span of the actuator. In this work two different variations on the serpentine configuration are evaluated: one constructed from patterned circular arcs and one from patterned rectangles. The influence of applied voltage is studied for the former case. To quantify these effects stereo particle image velocimetry (PIV) is used to generate time averaged, spatially resolved measurements of the detailed flow structure. The three components of the velocity vector are measured along spanwise and streamwise cuts. These slices are then reconstructed to provide a three-dimensional view of the induced flow field. The results for the induced flow fields are also compared with stereo-PIV measurements made on a standard linear DBD actuator. A truly three-dimensional induced flow field was observed as a result of the serpentine configuration. These designs could be beneficial for rapid mixing of the local fluid.

(Some figures may appear in colour only in the online journal)

1. Introduction

In recent years the dielectric barrier discharge (DBD) plasma actuator arguably received considerable attention due to its simplicity in design and potential operational benefits. Its operation requires a high voltage, alternating current (ac) source capable of peaks on the order of 5–10 kV. The high-voltage signal is then applied to a conducting electrode adhered to a dielectric substrate. A grounded electrode is placed asymmetrically on the lower surface of the dielectric with an additional dielectric layer covering it to avoid an unwanted discharge. The high potential difference between the two electrodes weakly ionizes the surrounding air. The presence of the plasma manifests itself as an induced body force on the fluid resulting in a tangential wall jet (figure 1(*a*)). The induced flow, in quiescent air, for the DBD actuator is generally a few meters per second.

Due to such a relatively small influence on the surrounding medium, the range of Reynolds numbers in which this basic design has been effective is relatively low [1–3]. In order to extend upon the operational usefulness of the actuators, numerous authors have investigated variations on the design and arrangement of the standard DBD plasma actuator. One such variation is the plasma synthetic jet actuator or PSJA [4]. The PSJA creates a vertical jet away from the dielectric surface. The jet is produced by arranging the exposed electrode in a closed loop such that opposing discharges are generated. When the induced flows from the two discharges collide they are directed upwards. An array of linear plasma synthetic jet actuators has been used as streamwise vortex generators. The actuators were used to effectively mitigate separation resulting from turbulent flow over a convex ramp [5] and hump [6]. Spatially distributed forcing and jet vectoring has also been investigated by Porter *et al* [7]. In these experiments vectoring was achieved using a set of two opposing plasma actuators of different strengths.

In contrast, the serpentine design ensures a fully three-dimensional flow control mechanism using a single actuator

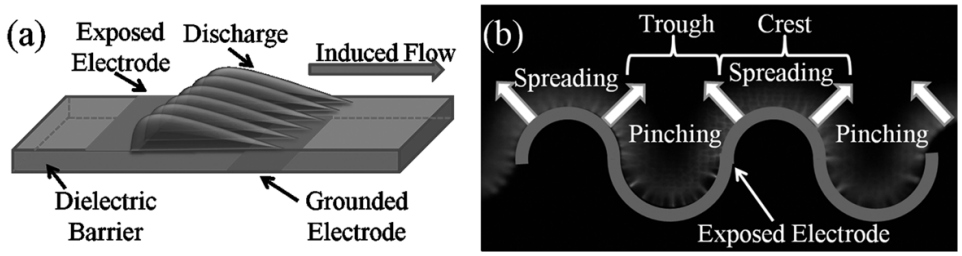

Figure 1. (*a*) A generic (standard) linear and (*b*) a circular serpentine DBD plasma actuator.

combining the effects of a standard linear actuator and a PSJA (figure 1(*b*)). Intuitively as one moves along the span of the actuator there is a spreading of the fluid at the crest while there is a pinching in the trough. Such a disturbance will result in an enhanced mixing of the surrounding fluid. This was first numerically proposed by Roy and Wang [8] who applied the actuator to modify flow over a flat plate. The results of the simulation also show similar vortex generating capabilities to that of the actuator configuration used by Schatzman and Thomas [5]. However, instead of using an array of actuators, only a single actuator is needed in the serpentine design. This could potentially lead to lower power consumption and less electrical circuitry. The serpentine configuration has also been explored numerically for the control of flows over a flapping [9] and stationary [10] airfoil representative of micro-air vehicle (MAV) applications. A congruent geometry was also used in a closed loop control system [11] on a morphing airfoil for stall sense and control for a subsonic turbulent boundary-layer (Mach 0.05 with a chord Reynolds number of 9×10^5). Although the underlying fluid dynamic mechanisms were not investigated, an improvement in lift of $\sim$10% was observed while a linear actuator (oriented along the span) was found ineffective.

The purpose of this study is to characterize the induced flow field generated by two different serpentine configurations in quiescent air. The first design is constructed from patterned circular arcs, and the second from patterned rectangles. The non-intrusive flow diagnostic technique of particle image velocimetry (PIV) is used to quantify the effects of these actuators. A stereo-PIV system is used to capture time averaged, spatially resolved data sets of the vector fields along spanwise and streamwise cuts. The two-dimensional planes are then reconstructed to give a three-dimensional view of the induced flow field structure. Comparisons with a linear actuator are made as well.

2. Experimental setup

2.1. Serpentine actuator fabrication and design

We use a photo-fabrication method to construct the continuous curved surfaces of the serpentine actuator. Such a method is widely used in the electronics community for in-house printed circuit board (PCB) fabrication. Sheets of copper tape with a nominal thickness of 0.07 mm were first adhered to both sides of the acrylic dielectric substrate which has a relative dielectric constant of 3.0. The thickness, t, of the acrylic was 3.0 mm. The desired electrode arrangement is transferred to the copper by exposing a photosensitive dry film adhered to the sheet. This results in a mask with the desired actuator design covering the copper tape. The actuator is then submerged in a ferric chloride bath to remove (via wet/chemical etching) the unwanted copper. The reminiscence of the adhesive glue left behind by the copper tape was removed using a solvent such as methanol or acetone.

General schematics of the two serpentine designs investigated in this work are shown in figure 2: one with patterned circular arcs (figure 2(*b*)), and one with patterned rectangles (figure 2(*c*)). For both designs tested, the width of the exposed electrode, w_1, was fixed at 2 mm and there was no horizontal displacement between the electrodes. In the patterned circular arcs design (figure 2(*b*)) the radii of the inner edge of the exposed electrode are 6 (r_1) and 4 (r_2) mm. The lower, grounded electrode in this design has a width, w_2, of 5 mm which follows along the inner radius of the exposed electrode. The dimensions for the patterned rectangular design are shown in figure 2(*c*) by $g_1 = 2r_1 = 12$ mm, $g_2 = r_1 + r_2 = 10$ mm, $g_3 = w_2 = 5$ mm and $g_4 = 2r_2 = 8$ mm. The grounded electrode for this design again follows along the windings of the exposed electrode but for simplicity of fabrication the excess grounded electrode was not removed in the trough region. The wavelength (p), or the length over which the pattern repeats itself, for both designs was 20 mm. To prevent end effects from influencing the velocity measurements, the actuators tested consisted of 8 and 9 wavelengths for the circular and rectangular designs, respectively. This corresponds to overall spanwise (z-direction) lengths, l_{span}, of 160 and 180 mm.

2.2. Plasma generation and power measurements

The high voltages required to ignite the plasma discharge were generated using a Corona Magnetics Inc. high-voltage transformer. A 10 kHz sinusoidal waveform was produced using a Tektronix arbitrary waveform generator (AFG3022B) and was further amplified using a QSC audio amplifier (RMX 2450). The voltage and current delivered to the actuator were monitored using a Tektronix high-voltage probe (P6015A) along with a Pearson Electronics ammeter (2100). The outputs from the probes were sampled at 250 MSa s^{-1} using a digitizing oscilloscope (Tektronix DPO3014). A 20.0 MHz low-pass filter was implemented on the oscilloscope for the channel

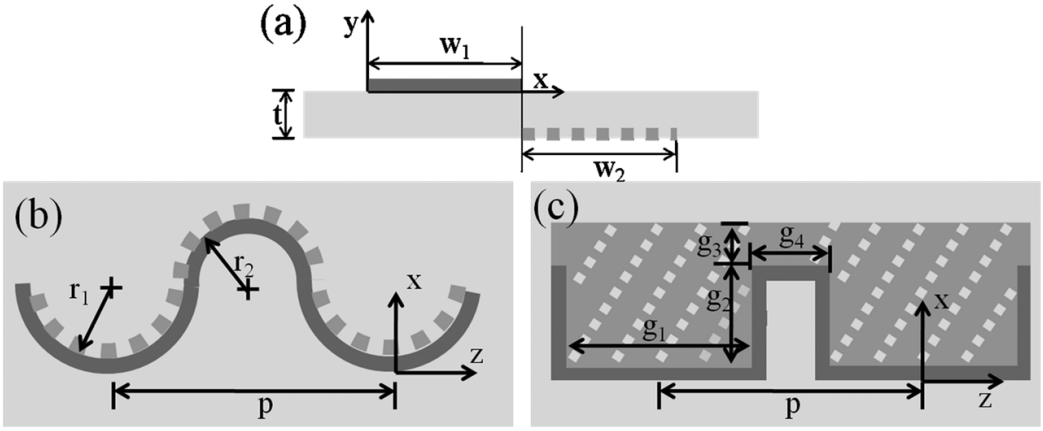

Figure 2. Schematics of the side (*a*) and top (*b*—circular, *c*—rectangular) views of the serpentine actuators tested.

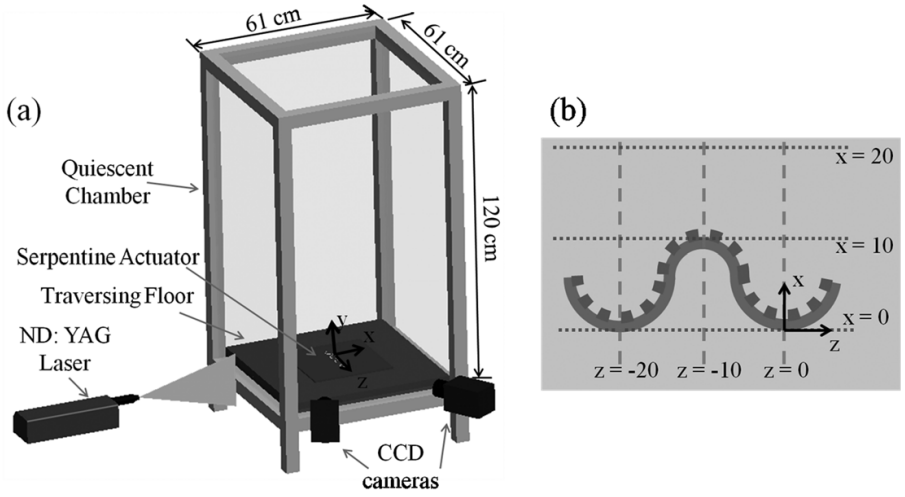

Figure 3. (*a*) The stereo-PIV setup and (*b*) locations of spanwise (dashed lines) and streamwise (dotted lines) planar cuts in mm.

connected to the current probe. In a single acquisition the oscilloscope captured 10^6 points. As such, 10 acquisitions were seized for each planar cut which corresponds to 400 periods over which the power delivered to the actuator is averaged. The total mean power, P_{tot}, was calculated by summing the product of the instantaneous voltage and current waveforms and dividing by the total number of points.

2.3. Particle image velocimetry

The standard linear plasma actuator is generally considered to be a two-dimensional device, indicating that the body force vector only has two components (x, y). This assumption does not hold, however, for the serpentine design. By nature of its configuration, fluid is pushed in all three directions. To capture these effects we use a stereoscopic PIV system to spatially resolve the three components of induced velocity vectors for a given two-dimensional plane.

The actuator is set up in a 61 × 61 × 120 cm quiescent chamber shown in figure 3(*a*). The floor of the chamber is connected to a single axis manual traverse (Velmex A1503P40-S1.5), which allows the floor to translate horizontally ±19 mm off centre. This eliminated the need to continuously readjust the stereo optics. Two of LaVision's ImagerPro X 4M (2048 × 2048 pixels) cameras in combination with 105 mm macro-lenses and 1.4× teleconverters were used to capture the PIV images. The cameras were aligned nearly perpendicular to the light sheet (figure 3) and had a relative angle of ∼58° between them. The field of view for each image was approximately 45 × 45 mm. A light sheet cutting along the actuator was generated using a Nd : YAG dual cavity pulsed 532 nm laser (New Wave Research Solo PIV II 30). A TSI atomizer (Model 9302) along with Ondina oil was used to seed the chamber. The atomizer produces a droplet with a mean diameter of ∼0.8 μm when pressurized at 25 psi [12]. Ondina is assumed to be dipole neutral and thus unaffected by the high electric field near the actuator.

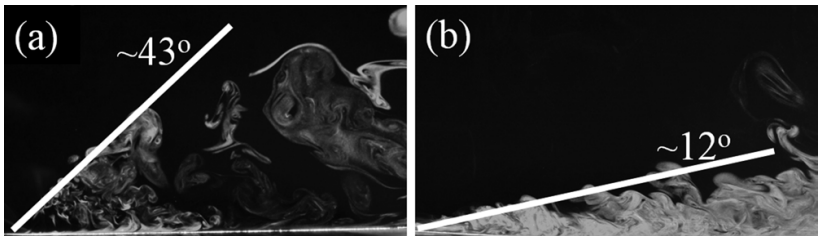

Figure 4. Smoke flow visualization: (*a*) circular patterned serpentine actuator (plane taken along the trough, $z = 0$ mm) and (*b*) standard linear actuator.

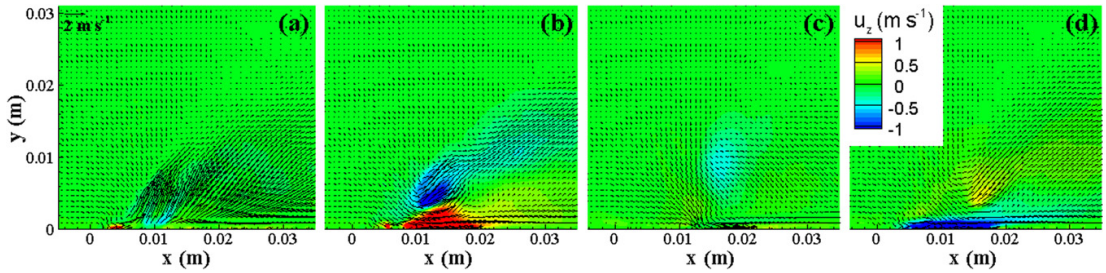

Figure 5. Time averaged z-velocity (m s^{-1}), u_z, contours overlaid with x and y-velocity vectors for various planar cuts along the span of a circular serpentine actuator (14 kV$_{pp}$). (*a*) $z = 0$ mm, (*b*) $z = -2.5$ mm, (*c*) $z = -10$ mm and (*d*) $z = -17.5$ mm.

LaVision's DaVis 7.2 3D-PIV software package was used to calibrate, capture, pre-process and process the PIV images. Image calibration was initially done with a 40 mm × 40 mm, two tiered calibration plate and was later refined using LaVision's self-calibration wizard [13]. A refining, multi-grid, stereo cross-correlation process was carried out on each image pair resulting in a final vector field resolution of 0.39 mm. To ensure statistical convergence of the velocity field, 200 image pairs were taken for each spanwise and streamwise cut. The vector fields were found to converge after ~150 acquisitions. Furthermore, for each planar slice two different time delays (between laser pulses), dt, were investigated. All results reported here are for a dt = 50 μs as there were no discernible differences from that of a 30 μs delay. Regardless of the time separations investigated, the resulting structure of the flow field remained essentially the same, with the average peak velocities varying no more than ~0.1 m s^{-1} for each case.

3. Results

In order to fully capture the three-dimensional nature of the induced flow field in the quiescent chamber, both spanwise and streamwise cuts were taken along two-dimensional planes of the actuator. For the spanwise cuts, nine planes were imaged starting at $z = 0$ mm and ending at $z = -20$ mm in -2.5 mm increments. Note that the total wavelength of the device is 20 mm; therefore a complete wavelength was captured in the spanwise scan. Similarly, 10 planes were captured in the streamwise direction starting at $x = -2.5$ mm and ending at $x = 20$ mm, again in 2.5 mm increments. Figure 3(*b*) provides an example of spanwise and streamwise planar cuts represented by dashed and dotted lines, respectively. The following section presents the results of these measurements and highlights how the serpentine (figure 2) design differs from that of a linear actuator (figure 1(*a*)).

3.1. Flow visualization

As a simple first step, the laser sheet was positioned to illuminate the spanwise plane cutting through the trough of circular serpentine actuator ($z = 0$ mm). A lit incense stick was placed ~5 mm upstream of the exposed electrode, the actuator was turned on, and the image was captured using a Nikon D90 SLR camera. The result of this rudimentary test indicates a vertically vectored momentum component along the plane. The flow is pushed away from the surface at approximately a 43° angle (figure 4(*a*)). As a comparison, smoke flow visualization with a standard linear actuator shows that the induced jet creates a ~12° angle with the surface (figure 4(*b*)). The observed pinching of the fluid in the serpentine configuration is a result of colliding streams of fluid accelerated due to the plasma body force. This force acts perpendicularly to the curvature of the exposed electrode driving the fluid parallel to the dielectric surface. However, since the serpentine design also consists of a neighbouring spreading region at the crest of the actuator the existence of a truly three-dimensional flow field is natural.

3.2. Circular serpentine actuator

If the serpentine actuator is truly a three-dimensional device, as one moves along the span of the actuator the z-component of velocity, u_z, and resulting flow structure should vary. This fact is shown in figure 5 which depicts contours of u_z for select spanwise locations for an input voltage of 14 kV$_{pp}$.

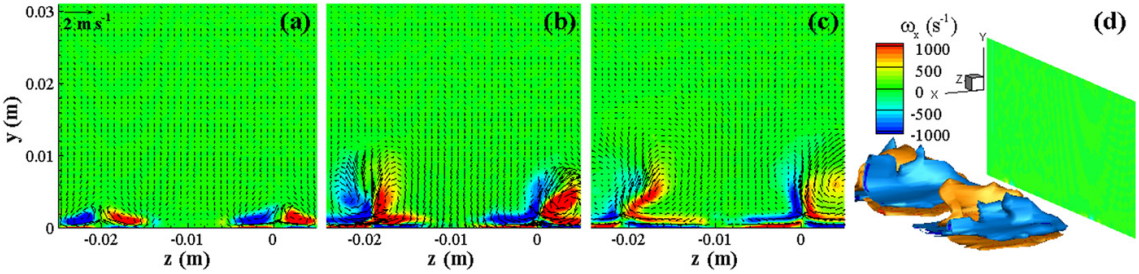

Figure 6. Time averaged contour plots and iso-surfaces of streamwise (ω_x) vorticity (s^{-1}) for a circular serpentine actuator with an input voltage of 14 kV_{pp}. (*a*) $x = 7.5$ mm, (*b*) $x = 12.5$ mm, (*c*) $x = 17.5$ mm and (*d*) a three-dimensional perspective view (the green plane indicates $x = 0$ mm).

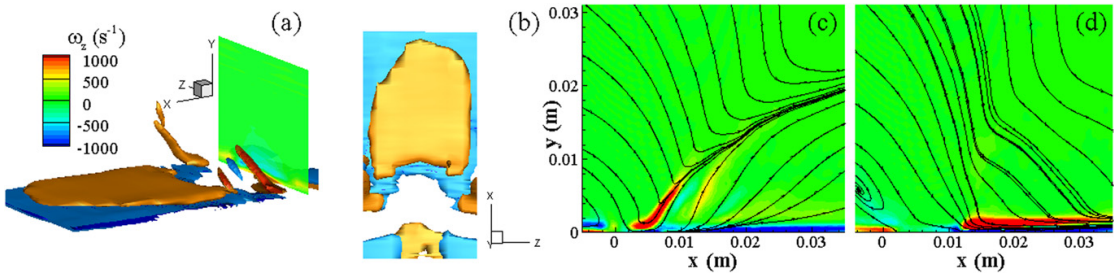

Figure 7. Averaged spanwise (ω_z) vorticity (s^{-1}) iso-surfaces reconstructed from planar measurements on a circular serpentine actuator (16 kV_{pp}): (*a*) perspective and (*b*) top views (the green plane indicates $x = 0$ mm). Contours and streamtraces extracted at (*c*) $z = 0$ and (*d*) $z = -10$ mm.

Figure 5 shows that at the trough ($z = 0$ mm) and the crest ($z = -10$ mm) of the actuator the flow direction is primarily in the x–y plane (or two-dimensional). For the other locations ($z = -2.5$ and -17.5 mm) presented in figures 5(*b*) and (*d*) one can see that the actuator is adding an out of plane component to the net momentum imparted to the fluid. It will be shown that this out-of-plane component results in streamwise counter-rotating vortex pairs (CVPs). The paired, anti-symmetric velocity contours in and out of plane shown in figures 5(*b*) and (*d*) are further evidence of the CVPs. Although the time average flow field at $z = 0$ mm and -10 mm shows no indication of a significant z-component in the velocity vector, an instantaneous image indicates a quite different scenario. Not shown here for brevity, a staggered structure in u_z was observed, which resulted in a net cancellation in the time average. Future efforts will address the temporal nature of this actuator configuration through phase locked stereo-PIV measurements.

Select results from the streamwise scan of the circular serpentine actuator are shown in figure 6, which depicts contours of the streamwise (ω_x) vorticity. These results show pairs of vectored counter-rotating vortices which are centred along the $z = 0$ and -20 mm planes (the troughs of the actuator). The vortices begin to form around the inflection point ($x = 6$ mm) of the curve making up the exposed electrode and continue to grow in magnitude as they propagate downstream. The growth of the vortex pairs is clearly seen in figure 6(*d*). These results agree well with prior numerical prediction [8] which showed the existence of such a flow structure. However, one may also notice the lack of symmetry between the vortex pair located at $z = 0$ mm and -20 mm. The asymmetry appears to worsen the further downstream. Such a result is most likely due to slight variations in the plasma body force along the span of the actuator which results in a non-uniformity in the flow field.

3.3. Effect of voltage for a circular serpentine actuator

To investigate the influence of input voltage on the structure of the induced flow, the supplied voltage was increased from 14 to 16 kV_{pp}. For voltages above 16 kV_{pp} the extension of the plasma began to approach the edge of the grounded electrode. At higher voltages this insufficient length in the grounded electrode could have resulted in a suppression of the plasma body force and the resulting velocity [14]. Higher voltages were therefore not investigated. Future experiments will address this limitation in the electrode arrangements. Figure 7 presents reassembled three-dimensional perspectives and planar contours of the time averaged spanwise vorticity (ω_z) for the higher driving potential. The results are similar to that found for the lower input voltage. The z-vorticity shows characteristics of a typical wall jet produced by a linear actuator (figure 11(*c*)) over most of the span of the device, with the exception being at the troughs ($z = 0$ and -20 mm). At these locations the opposing plasma forces results in a pinching of the fluid which is then propelled upwards. The only difference observed with the higher input voltage is an increase in vorticity strength particularly close to the wall. This increase is not

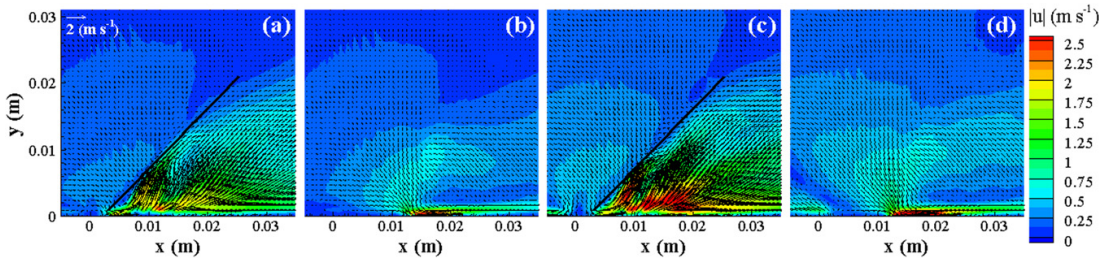

Figure 8. Time averaged velocity magnitude contours at the $z = 0$ mm and -10 mm planes along a circular serpentine actuator for input voltages of 14 kV_{pp} (*a*), (*b*) and 16 kV_{pp} (*c*), (*d*). The impingement angle in the flow was found to be $\sim 38^{\circ}$ as indicated by the black solid line.

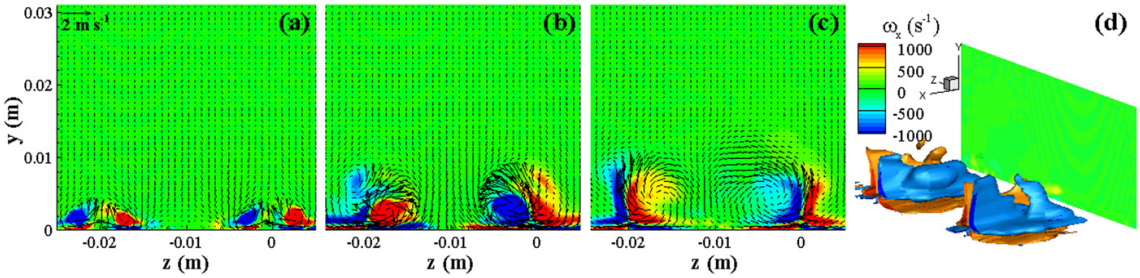

Figure 9. Time averaged contour plots and iso-surfaces of streamwise (ω_x) vorticity (s^{-1}) for a rectangular serpentine actuator (14 kV_{pp}): (*a*) $X = 7.5$ mm, (*b*) $x = 12.5$ mm, (*c*) $x = 17.5$ mm and (*d*) a three-dimensional perspective view (the green plane indicates $x = 0$ mm).

surprising given that the plasma force and its influence on the surrounding fluid velocity in known to increase with voltage for a DBD actuator. Thus, the spanwise vorticity component will increase close to a no slip wall.

An increase in velocity is indeed occurring as shown in figure 8. Despite this increase, the velocity profiles do not appear to change as figure 8 reveals for locations $z = 0$ and -10 mm. At the trough specifically, the resultant flow angle remains approximately at 38° as shown in figures 8(*a*) and (*c*) by a solid black line. This angle is in agreement with the angle estimated from flow visualizations described in figure 4 previously. This indifference to voltage on the impingement angle is not conclusive due to the limited range of voltage explored. It is, however, plausible. While the velocity of the impinging fluid is growing with increasing voltage it increases uniformly along the curvature of the electrode; pushing the fluid at a nominally constant angle. This would indicate that a segmented electrode structure with a variable voltage may be warranted for a truly controllable jet.

3.4. Rectangular serpentine design

The overall structure of the resultant flow field induced by the rectangular serpentine design with a 14 kV_{pp} input is remarkably similar to that of the circular configuration. However, there are a few notable differences starting with the streamwise vorticity generation. As figure 9 shows the rectangular design produces pairs of counter-rotating vortices centred about $z = 0$ mm and -20 mm, as well. The difference though lies in the strength and area over which the vortex acts. Since the rectangular design is made up of straight lines as opposed to the curved circular actuator, it is easy to see from figure 2(*c*) that a larger portion of the plasma generated along the actuator's wavelength will accelerate the flow in opposing z-directions. This results in additional streamwise vorticity generation.

The other noteworthy difference is in the magnitude of the resultant velocity at the trough and crest of the actuator (figures 10(*a*) and (*b*)). The structure of the flow at $z = 0$ and -10 mm is roughly identical to that found in figure 8. The impingement flow angle also remains constant at $\sim 38^{\circ}$. However, at $z = 0$ mm the velocity magnitude has increased compared with the circular serpentine design for the same input voltage, 14 kV_{pp}. The increase in velocity locally at the trough and not the crest is likely due to the straight line design and its influence on the out-of-plane velocity component.

The combination of both spanwise and streamwise vorticity generation creates a unique structure in the induced flow field for the serpentine configurations. As shown by the streamtraces in figures 10(*c*) and (*d*), which are reconstructed from the streamwise scan, the fluid follows a corkscrew like path as it is entrained in the troughs of the actuator. The vectored pinching of the fluid in this region pushes the fluid forward and away from the surface as u_z imparts a spin on its path. The fluid at the crest of the rectangular actuator is simply pushed forward. A similar corkscrew-like path was obtained from the spanwise scan, as well as for the circular serpentine design.

3.5. Comparison with a linear actuator

As a means of comparison, stereo measurements were made along the span of a standard linear DBD actuator as well.

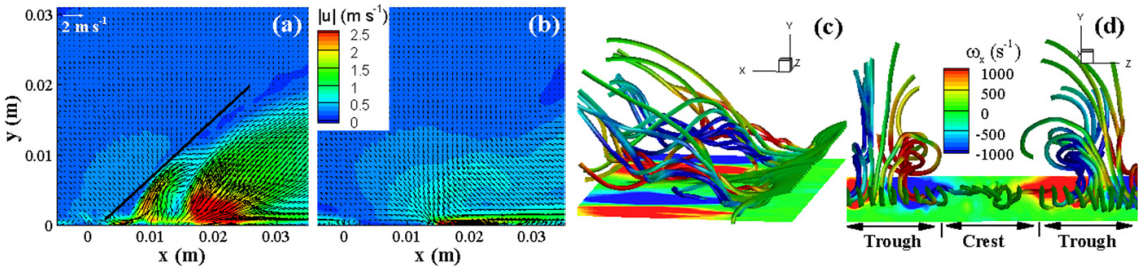

Figure 10. Time averaged velocity magnitude ($\mathrm{m\,s^{-1}}$) contours overlaid with x- and y-velocity vectors at (a) $z = 0$ mm and (b) $z = -10$ mm planes along a rectangular serpentine actuator (14 $\mathrm{kV_{pp}}$). The black solid line indicates the impingement angle in the flow, $\sim 38^{\circ}$. Streamtraces (c), (d) coloured by streamwise (ω_x) vorticity ($\mathrm{s^{-1}}$) showing a corkscrew-like structure in the induced flow field.

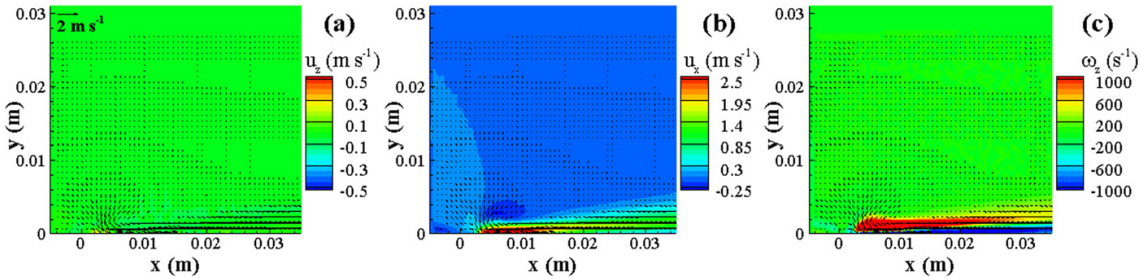

Figure 11. Time averaged quantities for a linear actuator driven at 14 $\mathrm{kV_{pp}}$ ($z = 0$ mm): (a) z-velocity ($\mathrm{m\,s^{-1}}$), (b) x-velocity ($\mathrm{m\,s^{-1}}$) and (c) z-vorticity ($\mathrm{s^{-1}}$).

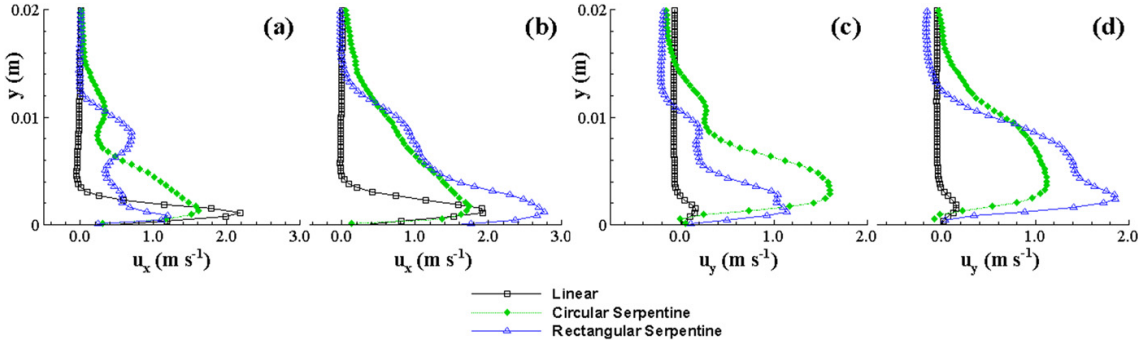

Figure 12. Velocity profiles of u_x ($\mathrm{m\,s^{-1}}$) and u_y ($\mathrm{m\,s^{-1}}$) taken at $x = 15$ mm (a), (b) and 20 mm (c), (d) for a linear, circular and rectangular serpentine actuator (14 $\mathrm{kV_{pp}}$). Plane taken along $z = 0$ mm for the serpentine cases.

Referring to figure 2(a), $w_1 = 2$ mm and $w_2 = 5$ mm for the electrode widths and the overall length, l_{span}, of the actuator was 160 mm. For this actuator only three planes ($z = 0$, -5, and -10 mm) were investigated all yielding approximately identical results. Z-velocity, x-velocity and z-vorticity contours along the $z = 0$ mm plane are shown in figure 11 for a 14 $\mathrm{kV_{pp}}$ input voltage. The velocity contours indicate that the out-of-plane component of velocity (u_z) is minute compared with that of the x-component. This validates the assumption that the linear actuator is a primarily two-dimensional device.

The u_x and u_y velocity profiles for two different spanwise locations ($x = 15$ and 20 mm) are presented in figures 12 and 13. The spanwise cuts for the serpentine cases were taken along the trough ($x = 0$ mm) in figure 12 while the cuts were taken at the crest ($x = 10$ mm) in figure 13. Both of these locations were shown above to be quasi-two-dimensional. The resulting profiles presented in figures 12 and 13 highlight key differences in the linear and serpentine designs. In the case of the linear DBD the momentum injection is primarily in the x-direction which is localized near the wall. As a result there are negligible vertical (y) or out-of-plane (z) components of velocity. The serpentine configuration, however, introduces both x, y and z (referring to figures 5 and 12) momentum to the fluid, particular at the trough. At the crest of the actuator (figure 13), the velocity profile of the serpentine

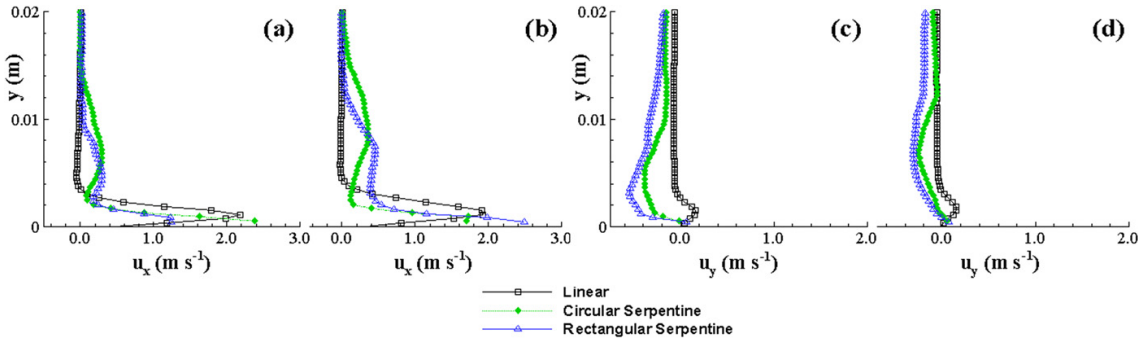

Figure 13. Velocity profiles of u_x and u_y taken at $x = 15$ mm (*a*), (*b*) and 20 mm (*c*), (*d*) for a linear, circular and rectangular serpentine actuator (14 kV_{pp}). Plane taken along $z = -10$ mm for the serpentine cases.

Table 1. Average power consumption for geometries tested (14 kV_{pp} input).

	P_{tot} (W)	P_{tot}/l_{span} (W m^{-1})	P_{tot}/l_{tot} (W m^{-1})
Linear	2.6 ± 0.5	16.3 ± 3.1	16.3 ± 3.1
Circular serpentine	4.8 ± 0.6	30.0 ± 3.7	19.1 ± 2.4
Rectangular serpentine	7.2 ± 0.8	40.0 ± 4.4	20.0 ± 2.2

actuators is comparable to the wall jet produced by the linear actuator.

The average calculated power consumption for each device is presented in table 1. When normalized by the spanwise length, l_{span}, the linear actuator clearly used the least amount of power, while the rectangular design consumed the most. However considering the total length of the electrode, l_{tot}, that accounts for the winding electrode, the normalized power variations between the designs drastically reduces. This result indicates that the ionization process may not be affected by the geometric manipulation of the electrodes. In the serpentine design one is only affecting the direction in which the plasma body force is oriented. However, from a design perspective, the ultimate goal is to apply these actuators to real-world aerodynamic flows such as over an airfoil. In such a case the actuator would most likely be applied over some unit length of the airfoil, where P_{tot}/l_{span} would be the more appropriate design parameter.

4. Conclusions

Stereo-PIV has been used to capture the complicated three-dimensional flow field induced by serpentine plasma actuators in a quiescent environment. Two different designs were investigated in this study: one constructed from patterned circular arcs and one from patterned rectangles. Both designs were found to inject x, y and z momentum resulting in three-dimensional vortical structures. In particular not only was spanwise vorticity generated but also counter-rotating vortex pairs in the streamwise direction. These vortex pairs were generated periodically along the span of the actuator. We note that the serpentine configuration combines the effects of a linear plasma synthetic jet actuator and that of a linear DBD actuator, both of which are inherently quasi-two-dimensional. As a result there is a vectored nature to the vortex generation in the serpentine design. This was shown to result in a corkscrew-like structure in the induced flow field. The serpentine actuators were further compared with a standard linear actuator where a nominally two-dimensional flow field was observed.

We believe that such a device has numerous aerodynamic applications where an increased mixing of the local fluid is desired. The areas of boundary-layer transition, convective heat transfer and plasma assisted combustion (PAC) all contain flow fields in which an improvement in flow turbulization could significantly enhance the desired output. An experimental study using a serpentine actuator on a freestream boundary layer of such an application remains open for evaluation in the near future. We expect the geometric design of the serpentine device would be strongly dependent on the boundary-layer characteristics of any given application. The influence on flow structure and controllable vectoring of a segmented serpentine design and the addition of a duty cycle to the supply voltage will be evaluated in future efforts.

Acknowledgments

This work was partially supported by AFOSR grant FA9550-09-1-0372 monitored by Dr Douglas Smith. The first author is also supported by a DOD SMART scholarship.

References

[1] Benard N, Braud P, Jolibois J and Moreau E 2008 Airflow reattachment along a NACA 0015 airfoil by surfaces dielectric barrier discharge actuator-time resolved particle image velocimetry investigation *4th Flow Control Conf. (Seattle, WA)* AIAA 2008-4202

[2] Huang J, Corke T C and Thomas F O 2006 Plasma actuators for separation control of low-pressure turbine blades *AIAA J.* **44** 51–7

[3] Sung Y, Kim W, Mungal M G and Cappeli M 2006 Aerodynamic modification of flow over bluff objects by plasma actuation *Exp. Fluids* **41** 479–86

[4] Santhanakrishnan A and Jacob J 2007 Flow control with plasma synthetic jet actuators *J. Phys. D: Appl. Phys.* **40** 637–51

[5] Schatzman D M and Thomas F O 2008 Turbulent boundary layer separation control with plasma actuators *4th Flow Control Conf. (Seattle, WA)* AIAA 2008-4199
[6] He C 2008 Plasma slats and flaps: an application of plasma actuators for hingeless aerodynamic control *PhD Thesis* Notre Dame
[7] Porter C, Abbas A, Cohen K, McLaughlin T and Enloe C 2009 Spatially distributed forcing and jet vectoring with a plasma actuator *AIAA J.* **47** 1368–78
[8] Roy S and Wang C 2009 Bulk flow modification with horseshoe and serpentine plasma actuators *J. Phys. D: Appl. Phys.* **42** 032004
[9] Rizzetta D P and Visbal M R 2011 Effect of plasma-based control on low-Reynolds number flapping airfoil performance *49th AIAA Aerospace Sciences Meeting. (Orlando, FL)* AIAA 2011-735
[10] Rizzetta D P and Visbal M R 2011 Numerical investigation of plasma-based control for low-Reynolds-number airfoil flows *AIAA J.* **49** 411–25
[11] Poggie J, Tilmann C P, Flick P M, Silkey J S, Osborne B A, Ervin G, Maric D, Mangalam S and Mangalam A 2010 Closed-loop stall control system *J. Aircraft* **47** 1747–55
[12] TSI 2000 Model 9302 Atomizer, Instruction Manual (St Paul, MN: TSI Inc.)
[13] 2007 DaVis 7.2, Instruction Manual (Göttingen, Germany: LaVision GmbH)
[14] Forte M, Jolibois J, Pons J, Moreau E, Touchard G and Cazalens M 2007 Optimization of a dielectric barrier discharge actuator by stationary and non-stationary measurements of the induced flow velocity: application to airflow control *Exp. Fluids* **43** 917–28